Materials Advances

ROYAL SOCIETY OF CHEMISTRY

PAPER

View Article Online
View Journal | View Issue



Cite this: *Mater. Adv.*, 2025, **6**, 6066

# Synthesis engineering and development of emergent conducting pi-conjugated materials: applications in energy harvesting and storage devices†

Germán D. Gómez Higuita, *[ab] João H. C. Bocchi,[a] Yosthyn M. Ariza Florez,[a] Gustavo G. Dalkiranis,[a] Bianca de Andrade Feitosa,[a] Diego Sousa,[a] Sara Luiza Gusso,[c] Marcos Luginieski,[a] João Vitor de Lima,[a] Rafael F. Santiago de Souza[a] and Gregório Couto Faria *[a]

The synthesis engineering and development of poly(3,4-ethylenedioxythiophene):poly(styrenesulfonate) (PEDOT:PSS) have revolutionized the field of conducting π-conjugated materials, offering a robust and versatile platform for energy harvesting and storage applications. By fine-tuning synthesis parameters and doping strategies, the optoelectronic properties of PEDOT:PSS can be tailored for specific optoelectronic applications. Here, we report on recent advancements in the synthesis engineering of PEDOT:PSS inks, specially developed for energy harvesting and storage devices. Of particular interest is the application of the synthesized PEDOT:PSS inks as p-type organic thermoelectric materials, hole-transport layers (HTLs) in organic solar cells (OSCs), and battery/supercapacitor electrodes. The PEDOT:PSS inks synthesized herein, based on the Louwet route, were compared with state-of-the-art commercially available PEDOT:PSS inks, demonstrating similar or superior performances. For thermoelectric generators (TEGs), our best formulation exhibited a Seebeck coefficient of approximately 12.6 μV $K^{-1}$, surpassing the 12.3 μV $K^{-1}$ of the commercial PEDOT:PSS ink (Clevios™ PH 1000). In OSCs, our HTL proprietary ink achieved efficiencies and photovoltaic parameters comparable to those of the well-known commercial Clevios™ P VP AI 4083. Similar results were obtained in energy storage devices, where the conductive PEDOT:PSS synthesized herein outperformed commercially available formulations, both in open-circuit voltage and in discharge tests. The insights presented in this manuscript underscore the critical role of fine-tuning and synthesis engineering in advancing high-performance and scalable energy harvesting and storage devices.

Received 29th June 2025,
Accepted 15th July 2025

DOI: 10.1039/d5ma00692a

rsc.li/materials-advances



## Introduction

The global energy matrix still relies predominantly on non-renewable sources. Indeed, over 75% of the world's energy production is derived from burning fossil fuels – namely, oil, coal, and natural gas – which are the primary contributors to global climate change and greenhouse gas emissions.[1] Moreover, the International Energy Agency (IEA) forecasts a 25% increase in global energy demand by 2040, intensifying the urgency for a transition towards cleaner and more sustainable energy sources.[2] This energy transition necessarily involves the development and expanded use of renewable sources, such as wind, solar, and thermoelectric technologies, to name a few.[3]

In this context, organic electronics (OE) have emerged as a promising platform for developing next-generation sustainable energy technologies, due to their low carbon footprint, environmentally friendly manufacturing processes, and compatibility with low-cost solution-based fabrication methods.[4,5] Among the vast palette of organic molecules and polymeric materials employed in OE, the most prominent is the well-known poly(3,4-ethylenedioxythiophene) (PEDOT), a conducting polymer derived from thiophene monomers. The combination of excellent mixed electron–ion conductivity and long-term stability justifies its prominent role within OE and beyond. PEDOT is typically obtained through the polymerization of EDOT monomers in the presence of polystyrene sulfonate (PSS), forming a

[a] *Instituto de Física de São Carlos (IFSC), Universidade de São Paulo (USP), São Carlos 13560-970, Brazil. E-mail: gcfaria@ifsc.usp.br*
[b] *E-mat Pesquisa e Desenvolvimento Ltda, São Carlos 13.561-235, Brazil. E-mail: german@e-mat.ind.br*
[c] *Departamento de Ciência e Engenharia de Materiais, Escola de Engenharia de São Carlos, Universidade de São Paulo (USP), São Carlos 13563-120, Brazil*

† Electronic supplementary information (ESI) available. See DOI: https://doi.org/10.1039/d5ma00692a

polyelectrolyte complex known as PEDOT:PSS.[6] Another remarkable advantage of PEDOT:PSS is its ability to tune its final properties *via* synthesis engineering processes.[7,8] Adjustments to electronic mobility and the doping level are also possible through the inclusion of secondary additives.[9–12] These tunable properties make PEDOT:PSS a highly versatile material, enabling its use across a broad range of applications, including energy harvesting and storage technologies.[4,6,13,14]

PEDOT:PSS is widely employed in energy harvesting devices, especially in organic solar cells (OSCs) and thermoelectric generators (TEGs). In OSCs, it acts as an effective hole transport layer (HTL), facilitating efficient charge extraction and work-function alignment, which leads to enhanced device performance.[15–18] Its high transparency in the visible spectrum, relatively high hole mobility, and favorable energy levels, combined with water solubility and low-temperature processing, make PEDOT:PSS a preferred HTL material.[19–21] In TEGs, PEDOT:PSS serves as a p-type material, leveraging the Seebeck effect, whereby a thermal gradient induces the flow of charge carriers from hot to cold regions.[22] The thermoelectric performance is typically described by the figure of merit $ZT = S^2 \cdot \sigma \cdot T/\kappa$, where $S$ is the Seebeck coefficient, $\sigma$ the electrical conductivity, $\kappa$ the thermal conductivity, and $T$ the absolute temperature.[22–24] Strategies to enhance the power factor ($S^2 \cdot \sigma$), such as acid post-treatment,[25] thermal annealing,[26] and secondary doping,[27] have been shown to significantly improve the conductivity of PEDOT:PSS without affecting the Seebeck coefficient.[24,28,29]

Beyond energy harvesting, PEDOT:PSS has also demonstrated great potential in energy storage systems, due to its ability to transport both ionic and electronic charges, along with its high electrochemical stability.[30,31] Indeed, PEDOT:PSS-based batteries have played an important role in the development of the field of neuromorphic electronics, as they formed the foundational concept behind organic neuromorphic devices.[32,33] These batteries operate by leveraging a doping asymmetry between two PEDOT:PSS electrodes separated by an electrolyte layer. One electrode remains oxidized (doped, PEDOT:PSS), while the other is dedoped, typically *via* treatment with polyethylenimine (PEI), either by dipping the electrode into a PEI solution[31] or by exposing it to PEI vapor.[32]

In the work presented here, we report on the synthesis engineering of a series of PEDOT:PSS inks specifically tailored for application in TEGs, OSCs, and polymer-based batteries. Our inks demonstrated similar or superior performance compared to leading commercial PEDOT:PSS formulations. For TEGs, our best formulation exhibited a Seebeck coefficient of (12.60 ± 0.06) μV $K^{-1}$, surpassing the (12.32 ± 0.06) μV $K^{-1}$ obtained with the commercial PEDOT:PSS ink Clevios™ PH 1000. In OSCs, the tailored inks achieved efficiencies and photovoltaic parameters comparable to those of the well-known commercial Clevios™ P VP AI 4083. Similar advantages were observed in energy storage devices, where our synthesized PEDOT:PSS outperformed PH1000 in both open-circuit voltage and discharge behavior. This study not only focuses on the optimization of the functional properties of conductive polymers but also highlights the growing role of Latin American research in developing sustainable and scalable materials for global energy technologies.

## Results and discussion

### PEDOT:PSS synthesis engineering

The synthesis of PEDOT:PSS inks was carried out following the strategy developed in our previous studies.[7,8] In these works, we modified the Louwet synthetic route by adjusting the molar ratio between the oxidizing agent and the EDOT monomer, allowing us to tune the charge density and electronic properties of the resulting PEDOT:PSS films.

Briefly, PEDOT:PSS inks were synthesized *via* the oxidative polymerization of 3,4-ethylenedioxythiophene (EDOT, Aldrich) in the presence of an aqueous solution of poly(styrene sulfonic acid) (PSS, $M_w \approx 75$ kDa, Aldrich) using either potassium persulfate ($K_2S_2O_8$, Aldrich) or sodium persulfate ($Na_2S_2O_8$, Aldrich) as an oxidizing agent, and $Fe_2(SO_4)_3 \cdot 5H_2O$ (Aldrich) as a coadjutant catalyst. The molar equivalents of $K_2S_2O_8$ or $Na_2S_2O_8$ relative to the EDOT monomer were varied from 0.5 to 5, which justifies their labels 0.5P, 1P, 2P, 3P, 4P, and 5P (see Table 1), hereafter referred to as the P-family PEDOT:PSS inks. The oxidant was added dropwise over several hours under a nitrogen atmosphere.

After polymerization, the dispersion was purified in a dialysis tube (Thermo Fisher, MWCO = 3.5 kDa) to remove residual reagents and unreacted monomers. The final concentration was adjusted to 1.2 wt% for all inks. The P-family PEDOT:PSS inks were tested in energy harvesting and storage devices and their performance was compared with that of state-of-the-art commercially available PEDOT:PSS inks, starting with thermoelectric generator applications.

### TEG applications

As already mentioned, PEDOT:PSS is a material widely studied for polymer-based thermoelectric applications. Generally, studies use solvents such as dimethyl sulfoxide (DMSO) or ethylene glycol (EG) to improve the thermoelectric properties of commercial PEDOT:PSS inks, a process known as secondary doping.[24,34–38] In this doping process, phase separation occurs between PEDOT and PSS molecules, leading to an increase in electrical conductivity without significantly affecting the Seebeck coefficient values.[36–39] Here, we studied the influence of PEDOT:PSS inks with varying doping levels on the Seebeck coefficient.

Table 1 Pre-synthesis stoichiometric ratios of PSS/EDOT and oxidizing salt/EDOT for P-family PEDOT:PSS inks

| Code | Pre-synthesis PSS/EDOT molar ratio [mmol $mmol^{-1}$] | Pre-synthesis ($K_2S_2O_8$ or $Na_2S_2O_8$)/EDOT molar ratio [mmol $mmol^{-1}$] |
|---|---|---|
| 0.5P | 0.522/0.275 = 1.9 | 0.139/0.275 = 0.5 |
| 1P | 0.522/0.275 = 1.9 | 0.275/0.275 = 1 |
| 2P | 0.522/0.275 = 1.9 | 0.550/0.275 = 2 |
| 3P | 0.522/0.275 = 1.9 | 0.834/0.275 = 3 |
| 5P | 0.522/0.275 = 1.9 | 1.392/0.275 = 5 |

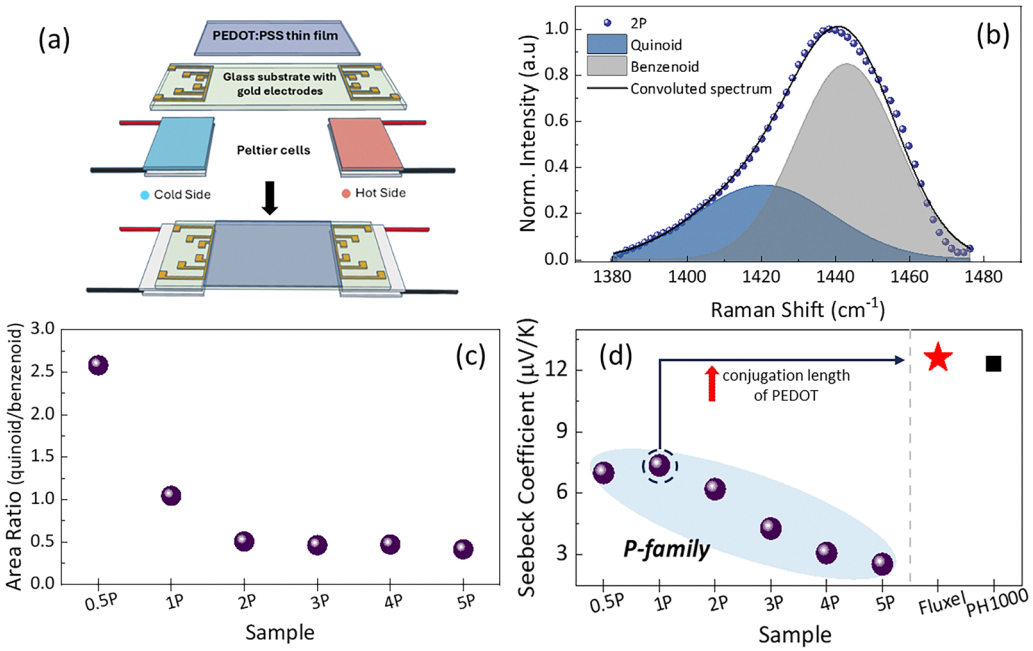


Fig. 1 (a) Scheme of the measuring system used to determine the Seebeck coefficient and electrical conductivity. (b) Deconvolution of the vibrational mode at 1438 $cm^{-1}$. (c) Ratio between the areas of quinoid and benzoid structure contributions. (d) The Seebeck coefficient of PEDOT:PSS inks. The uncertainty intervals are smaller than the data points.

For the thermoelectric characterization of PEDOT:PSS films, including Seebeck coefficient and electrical conductivity measurements, we used a lab-made system (Fig. 1a), as described in the Experimental section and detailed elsewhere.[40] We evaluated six PEDOT:PSS inks previously reported by our group and discussed in the Synthesis section (P-family PEDOT:PSS inks).[7] To verify the doping levels, Raman spectroscopy measurements were performed on the P-family inks (see Fig. S1, ESI†). By analyzing the vibrational mode around 1438 $cm^{-1}$ (Fig. 1b), corresponding to the symmetric stretching of the aromatic $C_\alpha{=}C_\beta$ bond, the relative contributions of the quinoid (doped) and benzenoid (neutral) structures – and thus the doping efficiency – could be assessed.[41] The vibrational mode was deconvoluted using Gaussian fit (Fig. 1b) and the area ratio of quinoid to benzenoid contributions was calculated (Fig. 1c). Fig. 1c shows that the 0.5P sample exhibits the highest doping level as it presents the highest contribution of the quinoid structure. Fig. 1d depicts the Seebeck coefficient values of each P-family PEDOT:PSS film sample. The 1P sample exhibited the highest Seebeck coefficient, approximately (7.36 ± 0.02) μV $K^{-1}$ among the P-family inks. Moreover, the samples synthesized with higher molar ratios of $Na_2S_2O_8$ to EDOT (such as the 5P ink) exhibited lower Seebeck coefficients, demonstrating that the Seebeck coefficient decreases with increasing oxidizing agent content during polymerization (see Table 1).

Electrical conductivity was determined by means of current–voltage (*IV*) measurements, from which the power factor (PF) of PEDOT:PSS was calculated (see Fig. S2, ESI†). Although the 0.5P sample exhibited the highest doping level (Fig. 1c), it showed the lowest carrier density (polaron and bipolaron intensities) among the analyzed samples, as indicated by UV-Vis-NIR spectroscopy (see Fig. S3, ESI†). This apparent contradiction is attributed to the lower conversion efficiency from EDOT to PEDOT in sample 0.5P due to the lower amount of oxidizing agent used during polymerization.[7] Conversely, the 2P sample demonstrated the highest electrical conductivity, approximately (10.83 ± 0.09) S $cm^{-1}$, attributed to its apparently higher carrier density (see Fig. S3, ESI†) resulting from a greater number of conductive PEDOT chains. The 1P sample achieved the highest PF, around (0.053 ± 0.001) μW $(K^2\ m)^{-1}$ (see Fig. S1, ESI†). These results suggest that, despite its lower conductivity compared to the 2P sample, the balanced interplay between the doping level and carrier density in the 1P composition was more favorable for maximizing the PF.

Since the samples exhibited lower Seebeck coefficients compared to the commercial PEDOT:PSS ink (Clevios™ PH1000, 12.32 ± 0.06 μV $K^{-1}$), a new ink was synthesized aiming to increase the conjugation length of the PEDOT chain, thereby increasing the Seebeck coefficient (as percolation would dominate the conductive mechanism as opposed to hopping processes).[42] Thus, the newly synthesized sample, named Fluxel, maintained the $Na_2S_2O_8$/EDOT molar ratio equal to 1, as the 1P sample exhibited the highest Seebeck coefficient, while reducing the molar ratio of EDOT to PSS.

FTIR and UV-Vis-NIR measurements (Fig. S4 and S3, respectively, ESI†) confirmed a higher degree of conjugation in the Fluxel ink compared to the 1P sample. In particular, the FTIR spectra reveal that the ratio between the infrared bands at 685 $cm^{-1}$ and 830 $cm^{-1}$, associated with the CH vibrations of mono- and di-substituted EDOT units, respectively,[43,44] was

lower than that observed for the 1P sample, indicating a higher degree of PEDOT polymerization (see Table S1, ESI†).[7,8] UV-Vis-NIR spectra further revealed increased absorption at wavelengths associated with bipolaron bands, consistent with a higher density of charge carriers. Raman analysis (Fig. S1, ESI†) suggests that the doping level of the Fluxel ink is similar to that of the 1P sample.

The increase in conjugation length led directly to an enhancement of the Seebeck coefficient. This behavior is expected, since these inks possess a low charge carrier density; thus, an increase in carrier concentration – and possibly mobility – due to the extended conjugation length contributes positively to the Seebeck coefficient.[24] Additionally, atomic force microscopy (AFM) analysis was also performed to compare surface morphology. The root mean square (RMS) roughness values obtained were 2.99 ± 0.31 nm for the Fluxel film and 0.87 ± 0.07 nm for the PH1000 reference, as shown in Fig. S5 (ESI†). Although both films exhibit relatively low RMS values, the Fluxel film is noticeably rougher, indicating that there is still room for improvement in solution processing – such as through the use and optimization of surfactant additives.

The Seebeck coefficient for the newly synthesized ink is presented in Fig. 1d (red star). It is noteworthy that the maximum Seebeck coefficient obtained for the Fluxel ink was (12.62 ± 0.06) μV $K^{-1}$, exceeding the value measured for a commercial PEDOT:PSS ink (Clevios™ PH1000), which was (12.32 ± 0.06) μV $K^{-1}$. Finally, the electrical conductivity of Fluxel was determined to be (78.04 ± 0.09) S $cm^{-1}$, leading to a PF of (1.24 ± 0.02) μW $(K^2\ m)^{-1}$.

## OSC applications

To investigate the performance of the PEDOT:PSS inks specifically synthesized for organic solar cells (OSCs), we employed them as hole transport layers (HTLs) in OSCs based on the PBDB-T-2F:Y6 system. A conventional device structure was used, consisting of glass/ITO/PEDOT:PSS/PBDB-T-2F:Y6/PFN-Br/Ag, as shown in Fig. 2a. The chemical structures of PBDB-T-2F and Y6 are depicted in Fig. 2b. The PBDB-T-2F:Y6 blend is widely recognized as the current benchmark in the OSC field, owing to its broad spectral absorption and efficient charge transport, with reported power conversion efficiencies exceeding 18%.[45] Its optimized energy levels and scalable processing also enable superior device stability and industrial relevance.

Initial tests were conducted by evaluating all the P-family PEDOT:PSS inks. It is worth mentioning that only the 0.5P ink exhibited acceptable performance and was thus selected for further investigation. We compared the PEDOT:PSS ink synthesized herein with three commercially available PEDOT:PSS inks specifically developed for HTL applications: Clevios™ P VP AI 4083,[46] Clevios P,[47] and HTL Solar.[48] These state-of-the-art PEDOT:PSS-based HTLs have been widely applied in the field of organic solar cells. The current density *versus* voltage (*J*–*V*) curves of the OSCs fabricated with the different PEDOT:PSS inks are presented in Fig. 2c, and the corresponding photovoltaic parameters are summarized in Table S2 (ESI†). Devices employing the 0.5P, Clevios™ P, and HTL Solar inks exhibited *J*–*V* characteristics with poor rectification behavior, limiting charge extraction and resulting in low fill factor (FF) values (below 60%). To overcome these limitations, we improved the formulation of the 0.5P ink by optimizing the PEDOT concentration, yielding a new ink denoted as Polaraci. Our Polaraci ink achieved a power conversion efficiency (PCE) of (13.6 ± 0.5)%, a short-circuit current density ($J_{SC}$) of (24 ± 1) mA $cm^{-2}$, an open-circuit voltage ($V_{OC}$) of (0.828 ± 0.004) V and an FF of (69.1 ± 0.8)%. These results are comparable to those obtained using the commercial Clevios™ P VP AI 4083 ink, which shows a

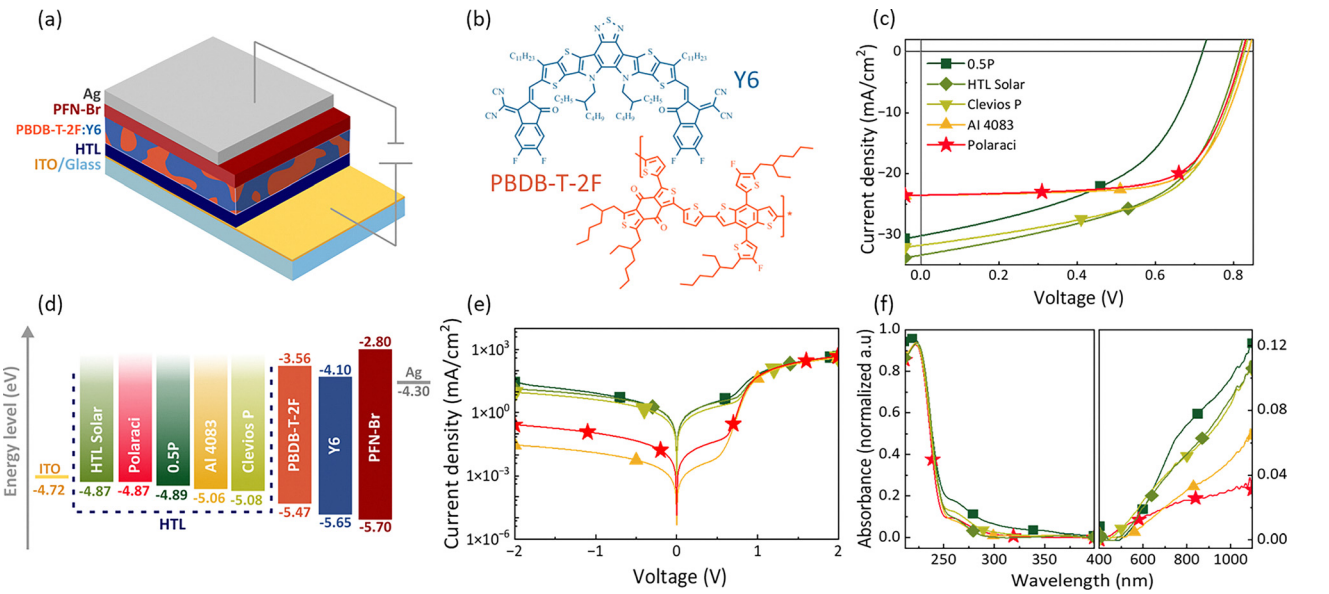


Fig. 2 (a) Device structure. (b) Chemical structures of PBDB-T-2F and Y6. (c) The light *J*–*V* curves of OSCs. (d) Energy level alignment of OSCs (the work function of the HTL variants was obtained experimentally through AFM by the Kelvin probe method). (e) Dark *J*–*V* curves of OSCs and (f) UV-Vis spectra of PEDOT:PSS inks used as HTLs in OSCs. The region between 400 nm and 1100 nm was re-scaled for better visualization.

PCE of (13.7 ± 0.5)%, a $J_{SC}$ of (23.5 ± 0.7) mA cm$^{-2}$, a $V_{OC}$ of (0.838 ± 0.004) V and an FF of (69.3 ± 1.5)%. The Polaraci and AI4083 present similar performance, except for a slight variation in open-circuit voltage ($V_{OC}$). This can be attributed to the work function differences between the Polaraci and Al 4083 (Fig. 2d), which influence the energy level alignment at the interface with the active layer, thereby affecting the built-in potential and ultimately the $V_{OC}$.[18,49,50]

The dark *J*–*V* characteristics, presented on a logarithmic scale in Fig. 2e, reveal that devices utilizing AI4083 and Polaraci as HTL layers exhibit lower reverse saturation current densities compared to those using Clevios™ P and HTL Solar. This result suggests a substantial suppression of current leakage, indicating more effective electron blocking and consequently leading to enhanced device performance and stability.[51–53] To investigate the origin of electron blocking differences between the PEDOT:PSS inks, we compared their UV-Vis absorption spectra individually, as shown in Fig. 2f. The results indicated that Clevios™ P, HTL Solar and 0.5P are inks with higher absorbance intensity of polarons (peak at 830 nm)[11,54] and bipolarons (peak beyond 1100 nm)[11,54] compared with AI 4083 and Polaraci. As the absorbance intensity is proportional to the concentration of absorbing species, it is fair to conclude that the inks that showed a lower FF present higher polaron/bipolaron density, implying an increase in electrical conductivity.[55] This higher conductivity could result in a reduced electron barrier and increased recombination rates within the hole transport layer of the device.[53,56]

Our Polaraci ink significantly outperforms the commercial Clevios P and HTL Solar widely used in the literature.[57–59] In addition, the material synthesized in this work exhibited standard deviations in PCE, $J_{SC}$, FF and $V_{OC}$ compared to AI4083, as shown in the box plot (Fig. 3), presenting equivalent reproducibility. Indeed, due to material and process instabilities, reproducibility in OSCs remains one of the major challenges in the research and development of this technology.[60,61] Additionally, AFM was used to compare the surface morphology of the HTL films. The RMS roughness values obtained were 0.68 ± 0.06 nm for the Polaraci ink and 0.75 ± 0.01 nm for AI4083 (Fig. S5, ESI†), indicating similarly smooth and homogeneous surfaces.

To study the charge dynamics within the devices, we analyzed the photocurrent density ($J_{ph}$) as a function of effective voltage ($V_{eff}$),[62,63] as presented in Fig. S6 (ESI†). $J_{ph}$ was determined from the light and dark current density–voltage (*J*–*V*) characteristics using the relation $J_{ph} = J_L - J_D$, where $J_L$ represents the current density under illumination and $J_D$ represents the current density under dark conditions. The effective voltage ($V_{eff}$) was calculated by subtracting the applied bias voltage ($V_A$) from the voltage $V_0$ ($J_{ph} = 0$).[64,65] The exciton generation rate ($G_{max}$) was extracted using the relationship $J_{sat} = q \times L \times G_{max}$, where $J_{sat}$ is the saturation photocurrent density, $q$ is the elementary charge, and $L$ is the active layer thickness. The dissociation probability ($P_{diss} = J_{SC}/J_{sat}$) and charge collecting probability ($P_{coll} = J_{MPP}/J_{sat}$) were calculated under short circuit conditions and at the maximum power point, respectively. The results are summarized in Table 2.

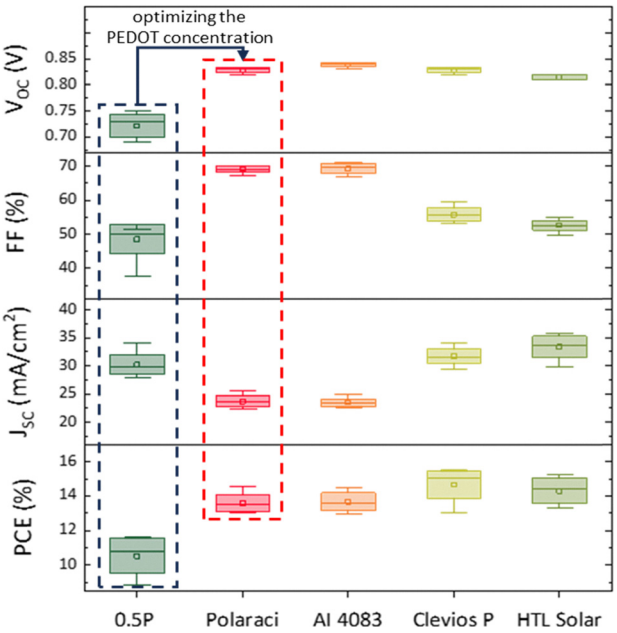


Fig. 3 Box plot illustrating the statistical distribution of the main photovoltaic parameters of the organic solar cells, $V_{OC}$, $J_{SC}$, FF and PCE. The value was calculated from the mean curve of 12 cells.

Table 2 Exciton generation rate ($G_{max}$), dissociation efficiency ($P_{diss}$) and charge collection efficiency ($P_{coll}$) of PBDB-T-2F:Y6 for PEDOT:PSS ink types

| Sample | $G_{max}$ (m$^{-3}$ s$^{-1}$) × 10$^{28}$ | $P_{diss}$ (%) | $P_{coll}$ (%) |
|---|---|---|---|
| 0.5P | 2.07 | 87.09 | 68.38 |
| Polaraci | 1.51 | 96.67 | 83.83 |
| AI 4083 | 1.50 | 97.48 | 85.94 |
| Clevios P | 2.16 | 91.67 | 73.86 |
| HTL Solar | 2.25 | 92.36 | 75.23 |

Clevios™ P, HTL Solar, and 0.5P exhibit higher exciton generation rates but suffer from reduced dissociation and charge collection efficiencies. This inefficiency suggests that, despite their superior light absorption and exciton generation capabilities, a significant fraction of excitons either fail to dissociate or recombine before contributing to the photocurrent, thereby reducing overall device performance. In contrast, AI 4083 and Polaraci exhibit comparable exciton generation rates as well as exceptionally high probability in both exciton dissociation and charge collection. The observed trends in $G_{max}$, $P_{diss}$, and $P_{coll}$ indicate superior performance for both HTLs, consistent with the higher $J_{SC}$ and FF values observed in the OSCs.[66,67] These favorable properties make AI 4083 and Polaraci ideal candidates for OSCs where minimizing recombination losses is crucial, as they efficiently convert generated excitons into free charge carriers and facilitate their collection at the electrodes.[68]

### Battery/supercapacitor applications

Polymer-based energy storage devices, such as batteries and supercapacitors, have been extensively proposed and studied in

the technical literature with great success.[31,69–72] A battery is an electrochemical device composed of two electrodes bridged by an electrolyte. Oxidation occurs on the anode electrode, where electrons are released. Reduction, conversely, takes place at the cathode, where electrons are accepted. The electrolyte facilitates ion movement between the electrodes to maintain charge balance while preventing direct electron flow. During the charging process, an external voltage applied between the two electrodes drives electrons from the cathode to the anode, while ions in the electrolyte migrate to maintain charge balance. This setup allows the battery to generate an electric current through controlled chemical reactions, making it a reliable energy storage and delivery system. During discharge, the stored chemical energy is converted back into electrical energy, with electrons flowing through the external circuit and releasing Gibbs free energy.[73]

The inks developed in this work are regarded as strong candidates for such applications, as fine-tuning the ratio of the EDOT monomer, PSS counterions, and the oxidizing agent enables precise control over the polymer's oxidation state. Here, we employ the synthesized PEDOT:PSS inks, with different doping levels, as anode electrodes, as a PEDOT:PSS-(PH1000)–PEI replacement. The structure of our battery device is shown in Fig. 4a. In all constructed battery devices, the cathode was fixed using the commercially available PEDOT:PSS (PH1000). On the other hand, our synthesized materials were applied as the anode material. PSSNa was used as an electrolyte. These devices were fabricated based on an initial selection of inks with varying ratios of EDOT and the oxidizing agent, following the same approach used in the TEG application section, in accordance with a previous study on neuromorphic devices from our group,[8] and referenced in the P family (Table 1). In a rechargeable battery, both electrodes must be reversible and stable upon successive oxidation and reduction reactions. Furthermore, achieving a higher $V_{OC}$ in batteries or supercapacitors requires a larger difference between the oxidation states of the electrodes. One of the strategies in the literature for controlling the oxidation state of organic PEDOT:PSS electrodes is the use of PEI. This compound plays a key role in stabilizing the oxidation level of PEDOT:PSS under air exposure. According to ref. 31 and 71, exposure to PEI allows for a partial reduction of PEDOT:PSS, converting some of its chains into the neutral state. This process reduces the oxidation level of PEDOT, a necessary condition to create a potential difference between electrodes, enabling battery operation.

However, the neutral state of PEDOT$^0$ is highly sensitive to atmospheric oxygen, making it prone to spontaneous reoxidation. PEI acts as a barrier against reoxidation, allowing batteries to exhibit a stable $V_{OC}$, reported to range from 0.5 V to 0.8 V.[31,71] Here, we applied the strategy of dedoping the anode electrode with PEI, as described in the Experimental section, to increase the difference in the oxidation levels between the electrodes. For comparison purposes, a device was constructed using the commercial PEDOT:PSS anode (PH1000), also dedoped with PEI, and will be referred to as PH1000 throughout this work. Once the devices were assembled, the open-circuit voltage ($V_{OC}$) was measured immediately and monitored for approximately 10 hours (Fig. 4b).

In Fig. 4b, we present the best-performing battery from the P family inks, referred to as 1P (Table 1), which exhibited a $V_{OC}$ of 0.52 V – well within the range reported in the literature. However, this value is slightly lower than that of the PH1000-based device, which reached 0.54 V under the same experimental conditions. Based on these results, we selected the 1P

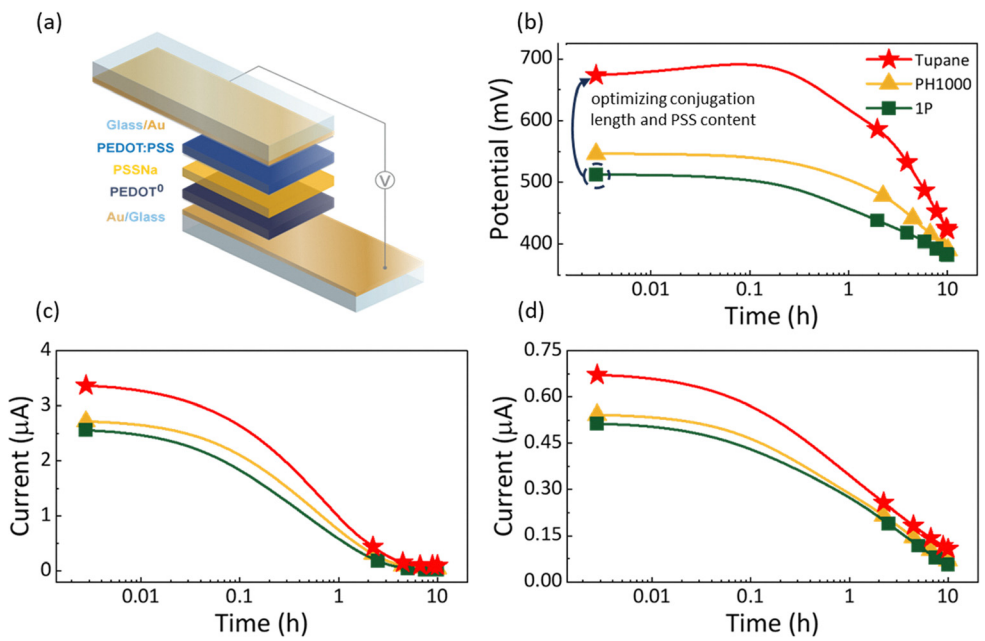


Fig. 4 (a) Schematic representation of battery/supercapacitor devices. (b) $V_{OC}$ of the characterized devices over 10 h. Discharge curves under (c) 200 kΩ and (d) 1 MΩ loads.

ink as a starting point to perform modifications in the synthesis process aimed at enhancing ion uptake. Here, the PEDOT conjugation length as well as the PSS content were optimized, resulting in the Tupane formulation. FTIR analysis (Fig. S4, ESI†) indicated a higher degree of conjugation in the Tupane formulation compared to the 1P ink, as evidenced by a lower 835/685 $cm^{-1}$ band intensity ratio. This trend is consistent with the interpretation discussed previously in the TEG section. Additionally, AFM measurements revealed an RMS roughness of $1.32 \pm 0.21$ nm for the Tupane film (Fig. S5, ESI†), suggesting a more textured surface that may facilitate ion–electrode interactions.

Such proprietary formulation enabled a battery with a $V_{OC}$ of 0.67 V – higher than that of the device based on commercial materials. Additionally, its potential increased to a maximum of 0.69 V within the first 10 minutes, before the discharge process began. This increase has been reported previously in other works and attributed to the continuous reduction of the PEDOT film in contact with PEI.[71] This effect might be associated with the drift of ionic species in the electrolyte towards the cathode and anode right after fabrication, increasing the double-layer capacitance at each electrode and, consequently, the open-circuit voltage. The better $V_{OC}$ observed might be associated with a larger difference in oxidation levels between the electrodes. Exposure to PEI vapor reduces the PSS chains, balancing with PEI evaporation byproducts and decreasing the concentration of $h^+$. This process lowers the Fermi level and conductivity. By comparing with a PH1000-based battery, we were able to show that, indeed, the control of the doping level of the anode changes the discharging time across distinct resistances of 200 kΩ and 1 MΩ (Fig. 4c and d, respectively), where the Tupane-based battery exhibited a better performance compared to the battery based on commercial materials. These results confirm that optimizing the oxidation level of PEDOT:PSS inks, especially through chemical formulations that better incorporate PEI treatment, is a key strategy for enhancing the performance of energy storage devices.

# Conclusions

The synthesis engineering approach discussed herein, based on varying synthesis parameters, such as temperature, time, cosolvent addition as well as distinct concentration of oxidation agents, enabled us to design the following PEDOT:PSS formulation, tailored for specific energy applications:

### For thermoelectric generators (TEGs)

The Fluxel formulation, derived from 1P, achieves the correct balance between electronic conductivity and thermal properties, enhancing the Seebeck effect. The Fluxel formulation exhibited Seebeck coefficients higher than that of the state-of-the-art commercially available ink PH100.

### For HTLs in OSCs

The Polaraci formulation, an ink derived from 0.5P, is characterized by good transparency, high efficiency in both exciton dissociation and charge collection. Our Polaraci formulation showed performances similar to the well-known Al4083, with superior reproducibility.

### For batteries

The Tupane formulation, also derived from 1P, was tailored for enhanced ionic conductivity and electrochemical stability, making it suitable as an electrode binder. Our Tupane formulation, when applied as an anode electrode, generated a higher open-circuit voltage, as well as higher charge retention as shown in the discharge curves, when compared to the traditional PH1000 structure.

# Experimental

### Fabrication and characterization of organic solar cells

The materials for device fabrication were sourced as follows: indium tin oxide (ITO) substrates were obtained from Xin Yan Technology Ltd. Poly[(2,6-(4,8-bis(5-(2-ethylhexyl)-4-fluorothiophen-2-yl)benzo[1,2-b:4,5-b′]dithiophene))-*alt*-(5,5′-(1,3-di(thiophen-2-yl)-5,7-bis(2-ethylhexyl)benzo[1,2-c:4,5-c′]dithiophene-4,8-dione))] (PM6, PBDB-T-2F) was acquired from Solarmer Materials, Inc. The non-fullerene acceptor (NFA) 2,2′-[[12,13-bis(2-ethylhexyl)-12,13-dihydro-3,9-diundecylbisthieno[2′,3′:4′,5′]thieno[2′,3′:4,5]pyrrolo[3,2-*e*:2′,3′-*g*][2,1,3]benzothiadiazole-2,10-diyl]bis[methylidyne(5,6-difluoro-3-oxo-1*H*-indene-2,1(3*H*)-diylidene)]]bis[propanedinitrile] (Y6, BTPTT-4F) was acquired from Luminescence Technology Corp. The electron transport layer (ETL) PFN-Br (poly(9,9-bis(3′-(*N*,*N*-dimethyl)-*N*-ethylammoinium-propyl-2,7-fluorene)-*alt*-2,7-(9,9-dioctylfluorene))dibromide) was acquired from Organtec Ltd (Beijing). The PEDOT:PSS variants, including AI4083, Clevios P, and HTL Solar, were supplied by Heraeus. The device fabrication process began with thorough cleaning of the patterned indium tin oxide (ITO) substrates. These substrates were first cleaned with detergent, followed by ultrasonic cleaning in Extran® MA 02, isopropyl alcohol, and acetone for 20 minutes each. The substrates were then subjected to UV-ozone surface treatment.

Aqueous dispersions of PEDOT:PSS (AI4083, HTL Solar, Polaraci and 0.5P) were applied to the treated substrates using dynamic spin-coating at 3000 rpm for 60 seconds. Following this, Clevios P was spin-coated at 6000 rpm for 60 seconds, and the layer was thermally annealed at 150 °C for 15 minutes, producing a PEDOT:PSS layer with a thickness of 30–35 nm. The prepared substrates were then transferred to a nitrogen-filled glovebox for further processing. The active layer was fabricated by spin-coating a PBDB-T-2F:Y6 mixture (weight ratio: 1 : 1.2, 16 mg $mL^{-1}$ in chloroform with 0.5 vol% chloronaphthalene) at 3000 rpm for 60 seconds.

The resulting film was then subjected to thermal annealing at 100 °C for 5 minutes to optimize its morphology. For the electron transport layer, PFN-Br (0.5 mg $mL^{-1}$ in methanol) was dynamically spin-coated onto the active layer at 4000 rpm for 30 seconds. Finally, a 120 nm thick layer of silver (Ag) was thermally evaporated as the top electrode under high vacuum

conditions ($\sim 2 \times 10^{-6}$ mbar) to complete the device structure. The active area of the device was 0.045 $cm^2$.

Device performance was evaluated under 100 mW $cm^{-2}$ illumination using a Solar Simulator Oriel Class AAA coupled with an AM 1.5G filter. *J–V* curves were acquired using a Keithley 2400 electrometer. UV-Vis spectroscopy measurements were conducted on thin films of quartz/PEDOT:PSS, prepared following the same procedures used for the solution and deposition of the layers in the cells, using a Hitachi U-2900 spectrophotometer.

### Atomic force microscopy (AFM) and work function determination

The AFM measurements were performed using a Bruker Dimension Icon system operating in tapping mode. A rectangular silicon cantilever with an oscillation frequency of 330 kHz and a spring constant of 40 N $m^{-1}$ was used for surface scanning.

To determine the work functions, thin films of the respective PEDOT:PSS samples were fabricated on ITO substrates *via* spin-coating, under the same conditions as those used for the preparation of this layer in the construction of the photovoltaic devices. The measurements were conducted using the Kelvin probe mode on an AFM, with a scan rate of 0.996 Hz, and the probe was calibrated using pyrolytic graphite. The AFM cantilever tip was an n-type antimony tip doped with silicon and subsequently coated with a 20 nm platinum–iridium layer. Measurements were performed using a Bruker Dimension Icon system.

### Raman spectroscopy

Raman spectra were acquired using a Renishaw inVia confocal Raman microscope equipped with a 532 nm polarized laser. The laser power was set to 1% of its maximum output, with an exposure time of 1 second per acquisition, and a total of 30 accumulations. Samples were prepared by drop-casting PEDOT:PSS ink solutions onto silicon (Si) substrates. The ink formulations included 0.1 vol% dodecylbenzene sulfonic acid (DBSA, Aldrich) as an additive. Following deposition, the samples were thermally treated at 100 °C for 10 minutes.

### Fourier transform infrared (FTIR) spectroscopy

FTIR spectra were acquired using a Thermo Nicolet NEXUS 470 spectrometer. Measurements were conducted on PEDOT:PSS films drop-cast onto clean silicon substrates, with spectral acquisition performed in the 1600–500 $cm^{-1}$ wavenumber range.

### Fabrication and characterization of thermoelectrics

The Seebeck coefficients were determined using a lab-made measuring system capable of applying a temperature difference and measuring the Seebeck voltage generated by the sample.[40] To establish a temperature gradient, two Peltier modules connected in reverse are used. A device with gold strips is used to measure the temperature difference applied to the sample while simultaneously measuring the voltage generated by the sample. Using the same system, without temperature gradient application, *IV* measurements were performed to obtain the electrical conductivity of the samples. To measure the Seebeck coefficient and electrical conductivity, thin films were deposited *via* spin-coating at 1000 rpm for 20 s. Before deposition, 5 vol% ethylene glycol (EG, Mallinckrodt) and 0.1 vol% dodecylbenzene sulfonic acid (DBSA, Aldrich) were added to the PEDOT:PSS solution. The thin films were annealed on a hotplate at 100 °C for 5 minutes.

### Fabrication and characterization of batteries

Solutions of PEDOT:PSS (PH1000) were prepared with 5 vol% EG, 0.1 vol% DBSA, 1 vol% of (3-glycidyloxypropyl)trimethoxysilane (GOPS), and PEDOT:PSS. A volume of 200 μL of the solution was cast onto clean glass/Au substrates and dried at 100 °C for 15 minutes. The electrode area was 2 $cm^2$. For the anode based on commercial PEDOT:PSS, the substrate with the cast film was exposed to PEI vapor at 250 °C for 5 minutes, as previously reported.[32] The preparation of batteries using our synthesized inks followed the same procedure as those prepared using commercial PEDOT:PSS. To compare the performance of our inks in batteries, our material was used as an alternative anode material.

A well made of PDMS was used to contain the electrolyte over the electrodes. PSS:Na gels were prepared as previously reported,[8] using poly(sodium-4-styrene sulfonate) (PSSNa, Aldrich, $M_w \approx 70$ kDa) (35 wt%), glycerol (Mallinckrodt) (10 wt%), D-sorbitol (Sigma) (20 wt%) and ultrapure Milli-Q water (35 wt%). The solution was mixed at room temperature for 1 h and then kept at room temperature for 24 h in a frasque to remove all air bubbles. Then, a small volume of this solution was dropped on the PDMS well on the anode. The substrate with the gel was dried on a hotplate at 50 °C for 10 minutes. Finally, the cathode was placed at the top of the PSSNa gel, forming a sandwich-like battery (see Fig. 4a).

All measurements were conducted right after assembly of the device under open air conditions. Immediately after the fabrication, the open circuit voltage was recorded with a Keithley 2182A nanovoltmeter for 10 h at 10-second intervals. In the sequence, the battery was recharged using a Keithley 2636b. The discharge potential was measured every 10 seconds over a period of 10 hours using 200 kΩ, 1 MΩ resistors and a nanovoltmeter. The corresponding discharge current was then calculated for each battery.

## Author contributions

G. D. G. H. conceptualized and synthesized the P-family materials, as well as the Fluxel, Polaraci, and Tupane inks. J. H. C. B. synthesized the materials and performed the TEG characterization and data analysis. Y. M. A. F., D. S., and S. L. G. performed the OPV characterization and data analysis. G. G. D. contributed to the TEG data analysis. B. A. F. and M. L. conducted the battery characterization and data analysis. J. V. L. was involved in the OPV characterization, and R. F. S. S. was involved in the battery characterization. G. C. F. supervised the materials synthesis and characterization studies, and oversaw the overall

project coordination. All authors contributed to the revision and editing of the manuscript.

## Conflicts of interest

Dr Germán D. Gómez Higuita is a founder at e-mat Pesquisa e Desenvolvimento Ltda, which produced the materials used in this study and holds their proprietary formulation (Fluxel, Polaraci and Tupane). The remaining authors declare that the research was conducted in the absence of any commercial or financial relationships that could be construed as a potential conflict of interest.

## Data availability

The data supporting this article have been included as part of the ESI.†

## Acknowledgements

The authors acknowledge funding from the Brazilian Federal Agency for Support and Evaluation of Graduate Education, CAPES finance code 001, by the São Paulo Research Foundation, FAPESP (grant numbers 2019/26375-7, 2022/02768-2 and 2023/10737-2), by the Brazilian National Council for Scientific and Technological Development, CNPq (grant numbers 446650/2024-2, 107555/2024-7, and 141507/2023-3), by the Pro-Rectorate for Inclusion and Belonging, PRIP/USP (grant number 23.1.6688.7.7) and the National Institute of Organic Electronics INEO/FAPESP/INCT (grant numbers 2014/50869-6 and 408449/2024-1).

## References

1 United Nations, Causes and Effects of Climate Change.
2 International Energy Agency, World Energy Outlook 2023, 2023.
3 International Energy Agency, The State of Energy Innovation, 2025.
4 J. R. Reynolds, B. C. Thompson and T. A. Skotheim, *Conjugated Polymers*, CRC Press, Boca Raton, 2019.
5 I. McCulloch, M. Chabinyc, C. Brabec, C. B. Nielsen and S. E. Watkins, *Nat. Mater.*, 2023, **22**, 1304–1310.
6 A. Elschner, S. Kirchmeyer, W. Lövenich, U. Merker and K. Reuter, *PEDOT Principles and Applications of an Intrinsically Conductive Polymer*, CRC Press, Boca Raton, 2011.
7 G. D. Gómez Higuita, F. Günther, B. C. Schroeder and G. C. Faria, *Polym. Chem.*, 2024, **15**, 3195–3203.
8 H. F. P. Barbosa, G. D. G. Higuita, F. Günther and G. C. Faria, *Adv. Electron. Mater.*, 2022, **8**, 2100864.
9 T. Murakami, Y. Mori and H. Okuzaki, *Trans. Mater. Res. Soc. Jpn.*, 2011, **36**, 165–168.
10 Q. Wei, M. Mukaida, Y. Naitoh and T. Ishida, *Adv. Mater.*, 2013, **25**, 2831–2836.
11 N. Massonnet, A. Carella, O. Jaudouin, P. Rannou, G. Laval, C. Celle and J. P. Simonato, *J. Mater. Chem. C*, 2014, **2**, 1278–1283.
12 J. Wang, K. Cai and S. Shen, *Org. Electron.*, 2015, **17**, 151–158.
13 I. Petsagkourakis, N. Kim, K. Tybrandt, I. Zozoulenko and X. Crispin, *Adv. Electron. Mater.*, 2019, **5**, 1800918.
14 X. Fan, N. E. Stott, J. Zeng, Y. Li, J. Ouyang, L. Chu and W. Song, *J. Mater. Chem. A*, 2023, **11**, 18561–18591.
15 F. Jin, R. Peng, Y. Qiu, J. Zhang and Z. Ge, *ACS Appl. Energy Mater.*, 2023, **6**, 9532–9542.
16 J. Xu, T. Heumüller, V. M. Le Corre, A. Barabash, R. Félix, J. Frisch, M. Bär and C. J. Brabec, *Joule*, 2024, **8**, 2570–2584.
17 H. Xu, F. Yuan, D. Zhou, X. Liao, L. Chen and Y. Chen, *J. Mater. Chem. A*, 2020, **8**, 11478–11492.
18 H. Tang, Y. Bai, H. Zhao, X. Qin, Z. Hu, C. Zhou, F. Huang and Y. Cao, *Adv. Mater.*, 2024, **36**, 2212236.
19 W.-M. Gu, K.-J. Jiang, X. Jiao, L. Wu, C.-Y. Gao, X.-H. Fan, L.-M. Yang, Q. Wang and Y. Song, *Chem. Eng. J.*, 2024, **485**, 149512.
20 V. D. Patel and D. Gupta, *Mater. Today Commun.*, 2022, **31**, 103664.
21 Q. Jiang, J. Tong, Y. Xian, R. A. Kerner, S. P. Dunfield, C. Xiao, R. A. Scheidt, D. Kuciauskas, X. Wang, M. P. Hautzinger, R. Tirawat, M. C. Beard, D. P. Fenning, J. J. Berry, B. W. Larson, Y. Yan and K. Zhu, *Nature*, 2022, **611**, 278–283.
22 D. M. Rowe, *Thermoelectrics Handbook: Macro to Nano*, CRC Press, 2005.
23 F. J. DiSalvo, *Science*, 1999, **285**, 703–706.
24 G.-H. Kim, L. Shao, K. Zhang and K. P. Pipe, *Nat. Mater.*, 2013, **12**, 719–723.
25 Y. Xia, K. Sun and J. Ouyang, *Adv. Mater.*, 2012, **24**, 2436–2440.
26 O. Bubnova, Z. U. Khan, A. Malti, S. Braun, M. Fahlman, M. Berggren and X. Crispin, *Nat. Mater.*, 2011, **10**, 429–433.
27 N. Kim, S. Kee, S. H. Lee, B. H. Lee, Y. H. Kahng, Y. Jo, B. Kim and K. Lee, *Adv. Mater.*, 2014, **26**, 2268–2272.
28 S. Liu, H. Li and C. He, *Carbon*, 2019, **149**, 25–32.
29 L. Wang, Z. Zhang, Y. Liu, B. Wang, L. Fang, J. Qiu, K. Zhang and S. Wang, *Nat. Commun.*, 2018, **9**, 3817.
30 P. R. Das, L. Komsiyska, O. Osters and G. Wittstock, *ECS Trans.*, 2015, **68**, 45–58.
31 Y. Xuan, M. Sandberg, M. Berggren and X. Crispin, *Org. Electron.*, 2012, **13**, 632–637.
32 Y. van de Burgt, E. Lubberman, E. J. Fuller, S. T. Keene, G. C. Faria, S. Agarwal, M. J. Marinella, A. Alec Talin and A. Salleo, *Nat. Mater.*, 2017, **16**, 414–418.
33 J. J. Yang and Q. Xia, *Nat. Mater.*, 2017, **16**, 396–397.
34 K.-C. Chang, M.-S. Jeng, C.-C. Yang, Y.-W. Chou, S.-K. Wu, M. A. Thomas and Y.-C. Peng, *J. Electron. Mater.*, 2009, **38**, 1182–1188.
35 M. Scholdt, H. Do, J. Lang, A. Gall, A. Colsmann, U. Lemmer, J. D. Koenig, M. Winkler and H. Boettner, *J. Electron. Mater.*, 2010, **39**, 1589–1592.
36 C. Liu, F. Jiang, M. Huang, R. Yue, B. Lu, J. Xu and G. Liu, *J. Electron. Mater.*, 2011, **40**, 648–651.

37 J. Luo, D. Billep, T. Waechtler, T. Otto, M. Toader, O. Gordan, E. Sheremet, J. Martin, M. Hietschold, D. R. T. Zahn and T. Gessner, *J. Mater. Chem. A*, 2013, **1**, 7576–7583.
38 M. Culebras, C. M. Gómez and A. Cantarero, *Materials*, 2014, **7**, 6701–6732.
39 D. A. Mengistie, C.-H. Chen, K. M. Boopathi, F. W. Pranoto, L.-J. Li and C.-W. Chu, *ACS Appl. Mater. Interfaces*, 2015, **7**, 94–100.
40 G. G. Dalkiranis, J. H. C. Bocchi, B. B. M. Torres, A. F. Lopeandia, O. N. Oliveira and G. C. Faria, *IEEE Trans. Instrum. Meas.*, 2025, 1.
41 A. Kanwat and J. Jang, *RSC Adv.*, 2016, **6**, 114800–114807.
42 R. Colucci, M. H. Quadros, F. H. Feres, F. B. Maia, F. S. de Vicente, G. C. Faria, L. F. Santos and G. Gozzi, *Synth. Met.*, 2018, **241**, 47–53.
43 A. J. Olivares, I. Cosme, M. E. Sanchez-Vergara, S. Mansurova, J. C. Carrillo, H. E. Martinez and A. Itzmoyotl, *Polymers*, 2019, **11**, 1–17.
44 Q. Zhao, R. Jamal, L. Zhang, M. Wang and T. Abdiryim, *Nanoscale Res. Lett.*, 2014, **9**, 1–9.
45 S. Shoaee, H. M. Luong, J. Song, Y. Zou, T. Nguyen and D. Neher, *Adv. Mater.*, 2024, **36**, 2302005.
46 D. H. Kim, D. J. Lee, B. Kim, C. Yun and M. H. Kang, *Solid State Electron.*, 2020, **169**, 107808.
47 M. Yi, S. Hong, J.-R. Kim, H. Kang, J. Lee, K. Yu, S. Kee, W. Lee and K. Lee, *Sol. Energy Mater. Sol. Cells*, 2016, **153**, 117–123.
48 A. Gregori, A. Tournebize, S. Schumann, H. Peisert, R. C. Hiorns, T. Chassé, C. Lartigau-Dagron and A. Allal, *Sol. Energy Mater. Sol. Cells*, 2018, **174**, 25–33.
49 M. Zhang, L. Zhu, G. Zhou, T. Hao, C. Qiu, Z. Zhao, Q. Hu, B. W. Larson, H. Zhu, Z. Ma, Z. Tang, W. Feng, Y. Zhang, T. P. Russell and F. Liu, *Nat. Commun.*, 2021, **12**, 309.
50 M. F. Lo, T. W. Ng, T. Z. Liu, V. A. L. Roy, S. L. Lai, M. K. Fung, C. S. Lee and S. T. Lee, *Appl. Phys. Lett.*, 2010, **96**, 113303.
51 B. Zhao, X. Huang, S. Chung, M. Zhang, Y. Zhong, A. Liang, Z. Zhao, C. Zhu, J. Zhao, S. Kim, J. Kim, M. Wang, S. Chen, K. Cho, Y. Wang and Z. Kan, *eScience*, 2024, 100305.
52 L. Jhamba, D. Wamwangi and Z. Chiguvare, *Opt. Quantum Electron.*, 2020, **52**, 245.
53 C. M. Proctor and T.-Q. Nguyen, *Appl. Phys. Lett.*, 2015, **106**, 083301.
54 I. Zozoulenko, A. Singh, S. K. Singh, V. Gueskine, X. Crispin and M. Berggren, *ACS Appl. Polym. Mater.*, 2019, **1**, 83–94.
55 J. L. Bredas and G. B. Street, *Acc. Chem. Res.*, 1985, **18**, 309–315.
56 F. Jin, Z. Su, B. Chu, P. Cheng, J. Wang, H. Zhao, Y. Gao, X. Yan and W. Li, *Sci. Rep.*, 2016, **6**, 26262.
57 S. Juillard, E. Planes, M. Matheron, L. Perrin, S. Berson and L. Flandin, *ACS Appl. Mater. Interfaces*, 2018, **10**, 29805–29813.
58 M. Karakawa, K. Suzuki, T. Kuwabara, T. Taima, K. Nagai, M. Nakano, T. Yamaguchi and K. Takahashi, *Org. Electron.*, 2020, **76**, 105448.
59 Abdullah, S.-J. Lee, J.-B. Park, Y.-S. Kim, A. Kotta and H.-K. Seo, *Synth. Met.*, 2024, **306**, 117619.
60 W. B. Tarique and A. Uddin, *Mater. Sci. Semicond. Process.*, 2023, **163**, 107541.
61 K. Fukuda, K. Yu and T. Someya, *Adv. Energy Mater.*, 2020, **10**, 2000765.
62 J. Gao, J. Wang, Q. An, X. Ma, Z. Hu, C. Xu, X. Zhang and F. Zhang, *Sci. China: Chem.*, 2020, **63**, 83–91.
63 C. F. N. Marchiori, Y. Garcia-Basabe, F. de, A. Ribeiro, M. Koehler, L. S. Roman and M. L. M. Rocco, *Spectrochim. Acta, Part A*, 2017, **171**, 376–382.
64 J. Qin, Q. Yang, J. Oh, S. Chen, G. O. Odunmbaku, N. A. N. Ouedraogo, C. Yang, K. Sun and S. Lu, *Adv. Sci.*, 2022, **9**, 2105347.
65 H. Feng, X. Song, Z. Zhang, R. Geng, J. Yu, L. Yang, D. Baran and W. Tang, *Adv. Funct. Mater.*, 2019, **29**, 1903269.
66 Y. Li, H. Xiang, J. Wang, B. Gao, J. Tang, C. Xiao, X. Wang and F. Wang, *J. Mater. Chem. A*, 2022, **10**, 23165–23174.
67 J.-D. Chen, C. Cui, Y.-Q. Li, L. Zhou, Q.-D. Ou, C. Li, Y. Li and J.-X. Tang, *Adv. Mater.*, 2015, **27**, 1035–1041.
68 S. M. Menke and R. J. Holmes, *Energy Environ. Sci.*, 2014, **7**, 499–512.
69 T. B. Schon, B. T. McAllister, P.-F. Li and D. S. Seferos, *Chem. Soc. Rev.*, 2016, **45**, 6345–6404.
70 C. Friebe and U. S. Schubert, *Adv. Energy Mater.*, 2015, **5**, 1500858.
71 M. Reyes-Reyes and R. López-Sandoval, *Org. Electron.*, 2018, **52**, 364–370.
72 E. Navarrete-Astorga, J. Rodríguez-Moreno, E. A. Dalchiele, R. Schrebler, P. Leyton, J. R. Ramos-Barrado and F. Martín, *J. Solid State Electrochem.*, 2017, **21**, 1431–1444.
73 K. Gurunathan, A. V. Murugan, R. Marimuthu, U. P. Mulik and D. P. Amalnerkar, *Mater. Chem. Phys.*, 1999, **61**, 173–191.